OPEN

NPG Asia Materials (2016) 8, e315; doi:10.1038/am.2016.150
www.nature.com/am

ORIGINAL ARTICLE

Ultrafast optical reduction of graphene oxide sheets on colorless polyimide film for wearable chemical sensors

Seon-Jin Choi[1,2], Sang-Joon Kim[2] and Il-Doo Kim[2]

Optically reduced graphene oxide (RGO) sheets were produced on a thermally stable and highly transparent colorless polyimide (CPI) substrate by irradiating intense pulsed light (IPL) on a GO-coated CPI film. These RGO sheets can be used as flexible gas sensing layers for wearable applications. Ultrafast IPL irradiation formed RGO sheets on the CPI film within 4 msec without any damage on the plastic substrate. The IPL-induced RGO (IPL-RGO) sheets exhibited dramatically improved chemical sensing performance toward H_2S, C_2H_5OH, and H_2, while the pristine GO sheets did not show any gas responses. In addition, consistent sensing properties were maintained even after the IPL-RGO sheets on the CPI film were mechanically deformed for 10^4 bending cycles. The gas responses of an IPL-RGO sensor toward H_2S, C_2H_5OH and H_2 were clearly distinguished by pattern recognition based on principal component analysis. Moreover, we successfully integrated our IPL-RGO sensor on a flexible printed circuit board with wireless Bluetooth communication and demonstrated outstanding sensing properties for potential applications in environmental and healthcare monitoring.

NPG Asia Materials (2016) **8,** e315; doi:10.1038/am.2016.150; published online 23 September 2016

INTRODUCTION

Wearable electronics represent technologies with potential applications in health and environmental monitoring. These electronics are noninvasive and automated personal devices that utilize the wireless transmittance of collected data containing the internal and external states of objects.[1,2] The development of essential components for wearable electronics has gained increased attention in recent years.[3] They include skin sensors for the detection of tactile and biological stimuli, strain sensors, pressure sensors, energy harvesters and heat generating elements.[4–9] Significant progress in wearable devices has been made in the flexibility and transparency of plastic substrates and in the ability to integrate materials for target applications. Recently, interests in healthcare and environmental monitoring have stimulated further development in chemical sensors with the capability for integration with wearable devices.[10,11] Generally, semiconductor metal oxide (SMO)-based sensing layers have been proposed and demonstrated for high performance chemical sensors.[12] In particular, nanostructured sensing materials with large surface areas and high porosity have been intensively studied with consideration that the sensing reactions mainly occur on the surface.[13–15] However, integration with flexible devices has been limited due to the inherently brittle property of SMO-based materials.

As an emerging chemical sensing layer, graphene has received more attention due to its robust mechanical stability and characteristic sensing property toward gaseous species.[16–18] Chemically and thermally reduced graphene materials have been employed as highly sensitive chemical sensing layers.[19,20] However, these chemical and thermal treatments typically require either use of toxic chemicals or are time-consuming processes. Moreover, these treatments have been limited to graphene coated on plastic substrates due to chemical or thermal damage to the substrate. As an alternative method, optical treatment has been proposed to modify the chemical state of graphene oxide (GO) by reducing the oxygen species at a relatively fast rate without damaging the plastic substrate.[21,22] Very recently, intense pulsed light (IPL) irradiation was introduced as an ultrafast optical treatment route for material sintering.[23,24] For example, Park *et al.*[25] demonstrated a very fast optical reduction of GO through flash light irradiation. However, to the best of our knowledge, optically reduced GO sheets have never been investigated on a flexible and transparent plastic substrate due to heat generation during light exposure, which can thermally deform plastic substrates.

To address this issue, the development of a new type of flexible and transparent substrate with high thermal stability has been pursued. Thus far, a number of polymer materials such as polyethylene terephthalate, polyimide (PI) and even paper have been explored as flexible substrates for wearable devices.[26–28] In particular, PI possesses superior thermal and mechanical stability. However, the poor transparency of PI limits broad applications for wearable electronics.[28,29] PI is known to exhibit a yellow–red color due to the charge transfer complex during the polymerization of polyamic acid (PAA).[30] To obtain a transparent PI film, it is essential to design appropriate monomer structures. For example, PAA can be synthesized by the

[1]Applied Science Research Institute, Korea Advanced Institute of Science and Technology, Daejeon, Republic of Korea and [2]Department of Materials Science and Engineering, Korea Advanced Institute of Science and Technology, Daejeon, Republic of Korea
Correspondence: Professor I-D Kim, Department of Materials Science and Engineering, Korea Advanced Institute of Science and Technology, 291 Daehak-ro, Yuseong-gu, Daejeon 305-701, Republic of Korea.
E-mail: idkim@kaist.ac.kr
Received 15 May 2016; revised 28 June 2016; accepted 2 August 2016

combination of an anhydride monomer and a diamine monomer that contains trifluoromethyl ($-CF_3$), sulfone ($-SO_2$) and ether (–O–) groups, which exhibit strong electronegativity, to reduce the charge transfer complex.[31] After the imidization of a properly designed PAA at an elevated temperature, a transparent PI film can be achieved.

Here, we used ultrafast IPL sintering for the optical reduction and functional modification of GO sheets, which were coated on a transparent PI substrate for application in flexible chemical sensors. A mechanically and thermally robust colorless PI (CPI) substrate was prepared for integration with a wearable sensor module. Then, GO sheets were drop-coated on the CPI substrate. The GO-coated CPI film was directly irradiated by IPL exposure to manipulate the electrical and chemical properties of GO by inducing reduced GO sheets (hereafter, IPL-reduced graphene oxide (RGO)). This process is highly robust and rapid; the IPL-RGO was achieved within 15 msec, thereby preventing damage to the CPI substrate. A dramatically enhanced gas sensing performance was obtained for H_2S, C_2H_5OH and H_2. In addition, the sensing properties were consistently maintained even when the film was in a mechanically altered shape. To demonstrate the potential use of the IPL-RGO on CPI film in wearable chemical sensors, we fabricated a flexible sensor module with the ability for wireless data transmission using Bluetooth and investigated its sensing performance for health and environmental monitoring.

MATERIALS AND METHODS

Materials

4,4′-(Hexafluoroisopropylidene)diphthalic anhydride (6FDA), 3,3′-diaminodiphenyl sulfone (APS), *N,N*-dimethylformamide and GO dispersed in a DI solution (2 mg ml^{-1}) were purchased from Sigma-Aldrich (St Louis, MO, USA). All chemicals were used without further purification.

Preparation of CPI film

As a precursor for CPI, PAA solution was prepared by dissolving 2.0365 g of 4,4′-(hexafluoroisopropylidene)diphthalic anhydride (6FDA) and 1.0180 g of 3,3′-diaminodiphenyl sulfone (APS) in 4 g of *N,N*-dimethylformamide solution. For complete dissolution, the mixture was stirred at 500 r.p.m. with a magnetic stirrer for 5 h at room temperature. The homogeneously dissolved PAA solution was coated on a glass substrate (2 cm × 2 cm) with a doctor's blade with a thickness range of 25–30 μm. A CPI film was achieved after imidization at 100 °C, 200 °C and 300 °C for 1 h at each temperature in a box furnace.

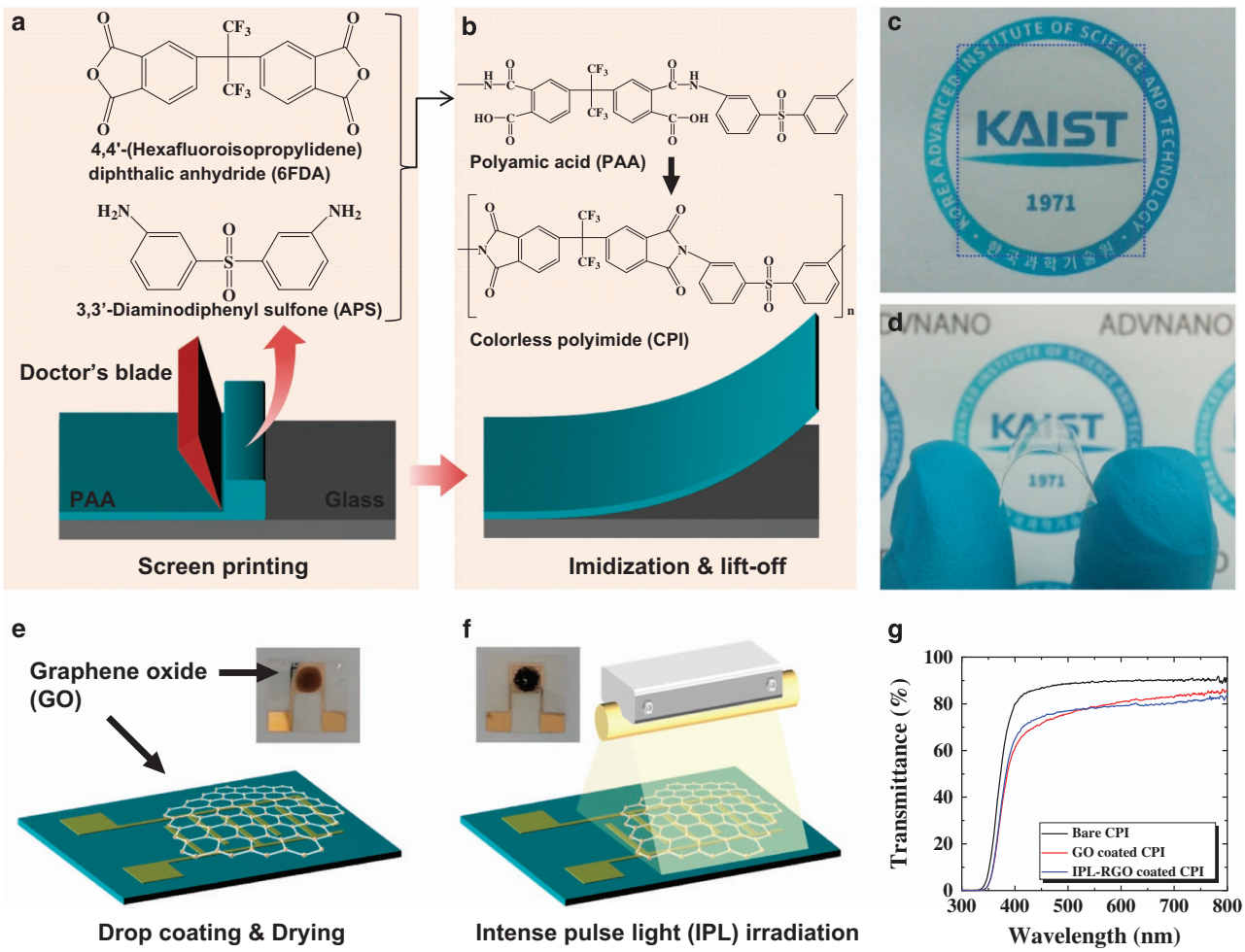

Figure 1 Schematic illustrations of (**a**) polyamic acid (PAA) synthesis using 4,4′-(Hexafluoroisopropylidene)diphthalic anhydride (6FDA) and 3,3′-diaminodiphenyl sulfone (APS), and screen printing using a doctor's blade on a glass substrate, and (**b**) imidization of PAA to form colorless polyimide (CPI) film and lift-off the CPI film on the glass substrate. Optical images of (**c**) the flat and (**d**) bent CPI film. Schematic illustrations of (**e**) graphene oxide (GO) sheets coated on CPI film with interdigitated electrodes (IDEs) pattern and (**f**) intense pulse light (IPL) exposure on GO-coated CPI film to form IPL-RGO on CPI film. (**g**) Transmittance of bare CPI film, GO-coated CPI film and IPL-RGO-coated CPI film without IDE pattern.

Interdigitated electrode patterning

Interdigitated electrodes (IDEs) were patterned on CPI film to measure resistance changes of pristine GO and IPL-RGO during exposure to different analytes. The IDEs on CPI film were patterned using a shadow mask with a finger width of 200 μm, a length of 2750 μm and a 200-μm spacing between electrodes. A 10-nm/100-nm-thick Ti/Au layer was deposited by thermal evaporation.

GO coating on CPI film

The GO-coated CPI film was prepared by drop-coating the GO dispersed DI solution. A 2 mg ml^{-1} concentration of the commercialized GO dispersed solution (Sigma-Aldrich) was used. A 5 μl GO solution was drop-coated on the Au IDE patterned CPI film using a micropipette and dried in ambient air.

Intensive pulsed light irradiation

A xenon flash lamp (ILC Technology, L6755) was used as a light source with the spectrum ranging from approximately 400 to 1100 nm. The pulsed light was introduced into the samples through quartz. The light energy was adjusted by modulating the applied voltage, pulse on/off time, pulse duration, pulse number and pulse gap. The GO-coated CPI film was placed under the quartz at a pulse gap of 5 mm. The pulse on/off time was fixed as 15 msec/30 msec. A high voltage of 150 V was applied to the flash lamp to control the flash light energy at 1.15 J cm^{-2}. A single-light pulse irradiated the GO-coated CPI film to form IPL-RGO.

Gas sensing characterization

The gas sensing characteristics were evaluated using a homemade measurement setup. All sensors were stabilized in baseline ambient air before the measurement. The sensors were exposed to different analytes (that is, hydrogen sulfide, ethanol and hydrogen) with concentrations ranging from 1–20 p.p.m. Each analyte was exposed for a certain number of minutes, followed by exposure to baseline air to recover the sensors. Resistance changes were measured using a data acquisition system (34 972A, Agilent). The relative resistance transition ($\Delta R/R_{gas} \times 100\%$) was measured, where R_{air} is the sensor baseline resistance upon exposure to air. In addition, ΔR is the resistance difference, either R_{gas}–R_{air} or R_{air}–R_{gas}, where R_{gas} is measured upon exposure to the different analytes. All measurements were performed at room temperature.

RESULTS AND DISCUSSION

The synthesis schemes for the CPI film and the IPL-RGO sheets are shown in Figure 1. PAA solution consisting of anhydride monomers of 4,4′-(hexafluoroisopropylidene)diphthalic anhydride (6FDA) and diamine monomers of 3,3′-diaminodiphenyl sulfone (APS) was selected to reduce the charge transfer complex (Figure 1a). The PAA solution was coated on a glass substrate by screen printing. Then, a thin CPI film was obtained after the imidization of the PAA solution (Figure 1b). The CPI film was peeled off from the glass substrate and used as a flexible substrate for fabricating the IPL-RGO sensors. The CPI film exhibited a high optical transparency and outstanding flexibility (Figure 1c and d). In addition, there was a minor difference between the decomposition temperatures (T_{onset}) of the CPI film (549 °C) and the commercial yellow PI film (576 °C), which demonstrated the high thermal stability of our CPI film (Supplementary Information, Supplementary Figure S1). After patterning IDEs on the CPI substrate, a GO solution was drop-coated onto the CPI film (Figure 1e). The GO-coated CPI film was placed under a light source to transform the GO to RGO by IPL irradiation (Figure 1f). The IPL irradiation is very powerful process because the whole process was finished within 15 msec without damaging the CPI film. To evaluate the transmittance property, bare CPI film, GO-coated CPI film and IPL-RGO-coated CPI film without IDE patterning were investigated (Figure 1g). The bare CPI film had an average thickness of 30 μm and exhibited a very high transmittance above 89% at 550 nm. However, after GO coating the CPI film, a slightly reduced transmittance of 78%

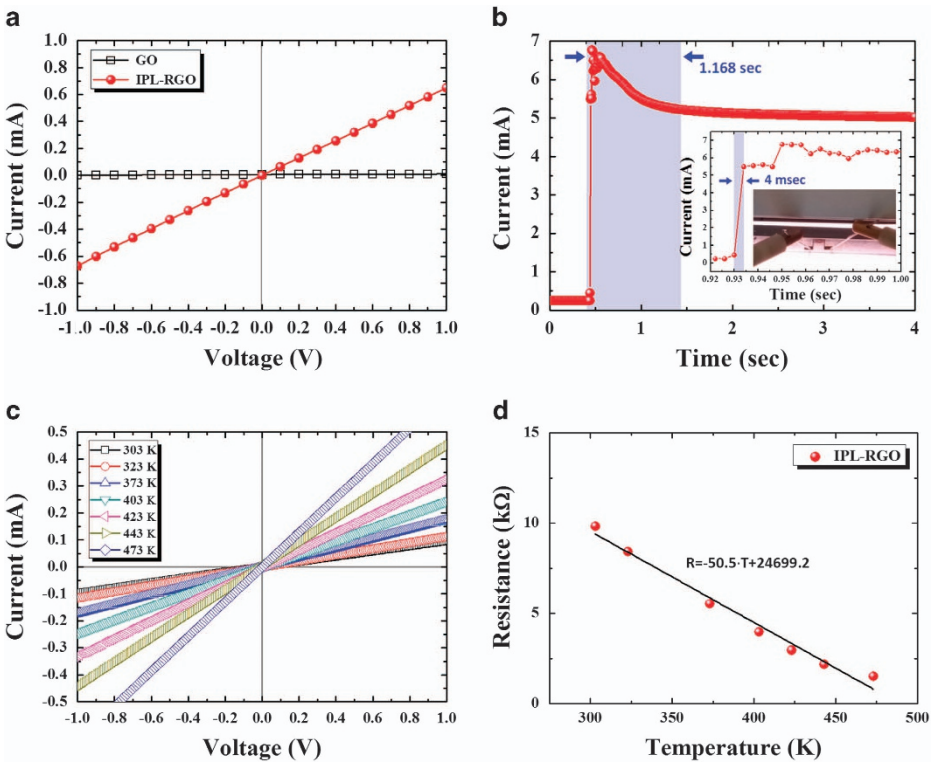

Figure 2 (**a**) I–V characteristics of graphene oxide (GO) and intense pulsed light-reduced graphene oxide (IPL-RGO) sheets on CPI film. (**b**) Real-time transition of electrical current after IPL irradiation. (**c**) I–V characteristics of IPL-RGO sheets at different temperatures. (**d**) Negative coefficient (50.5 Ω K^{-1}) of thermal resistivity investigated by resistance-temperature plotting.

was observed. The optical transmittance of the IPL-RGO-coated CPI film was 78%, similar to that of the GO-coated CPI film at 550 nm. Although the transmittance noticeably decreased after the GO coating and IPL irradiation, the value could be improved by carefully controlling the thickness of GO sheets on the CPI film.

The transition of electrical properties was investigated using the GO and IPL-RGO sheets to understand the effect of IPL irradiation (Figure 2). The electrical conductivity was significantly increased by IPL irradiation on the GO sheets (Figure 2a). An approximately 100-fold enhancement in electrical conductivity was observed with IPL-RGO compared with pristine GO. The real-time transition in electrical property was investigated during IPL irradiation (Figure 2b). There was a sudden increase in the electric current after the IPL irradiation. Then, the current slowly decayed for 1.168 s and subsequently saturated at a certain current. The dramatic enhancement in current occurred within 4 msec, reaching the peak current value (in the inset of Figure 2b). The temperature-dependent electrical property revealed that IPL-RGO exhibited an increasing current with respect to temperature from 303 K to 473 K, which indicated a semiconducting behavior of the IPL-RGO (Figure 2c). A linear approximation of the resistance-temperature plot revealed a negative coefficient ($50.5\ \Omega\ K^{-1}$) for the thermal resistivity of IPL-RGO (Figure 2d). The semiconducting property of RGO was consistent with a previous study.[32]

The effect of chemical modification was investigated to further understand the transition in the chemical binding states of IPL-RGO (Figure 3a-c). A pristine CPI film was initially examined by X-ray photoelectron spectroscopy (XPS) at C1*s* spectra (Figure 3a). The pristine CPI film exhibited two distinctive characteristic peaks at 284.71 eV and 285.38 eV, which corresponded to C–N and C–C/C = C bonds, respectively. The high intensity of the C–N peak at 285.38 eV was attributed to the chemical bonding of pristine CPI film. Then, the chemical binding states of the GO and IPL-RGO sheets were compared using XPS at C1*s* spectra (Figure 3b and c). A characteristic peak representing the C–C and C = C bonds was observed at the binding energy of 284.6 eV. In addition, characteristic peaks of various functional groups such as C–N, C–OH, C = O and O = C–OH were observed at 285.4 eV, 286.0 eV, 287.6 eV and 288.9 eV, respectively, which were consistent with previous observations for GO sheets.[33] The characteristic peak of C–N was ascribed to the chemical bonding of the CPI film underneath the thin GO sheets. However, an overall reduction in the intensities of the functional groups was observed, including a major reduction of the C = O peak intensity at 286.7 eV after the IPL irradiation of the GO sheets (Figure 3c). In addition, the estimated C1*s*/O1*s* ratio increased to 7.97 with IPL-RGO when compared with that of GO (C1*s*/O1*s* ratio = 1.95), which indicated the reduction of oxygen functional groups in the IPL-RGO sheets. Moreover, the characteristic peak of C–N was not present after IPL irradiation. This could be due to the volumetric expansion of IPL-RGO due to the formation of pores between the IPL-RGO layers and limited penetration depth of the X-ray source. Additional XPS analyses for pristine CPI film, GO and IPL-RGO specimens are presented in the Supplementary Information (Supplementary Figures S2 and S3).

The Raman spectra of the GO and IPL-RGO sheets exhibited two characteristic peaks (Figure 3d). The D band peak at 1352 cm^{-1} indicates a defect formation in the graphene due to oxidation, whereas the G band peak at 1594 cm^{-1} corresponds to the first-order scattering of the E_{2g} mode of the sp^2 domains in the GO sheets.[34] Similarly, the D and G band peaks of IPL-RGO sheets were observed at 1349 cm^{-1}

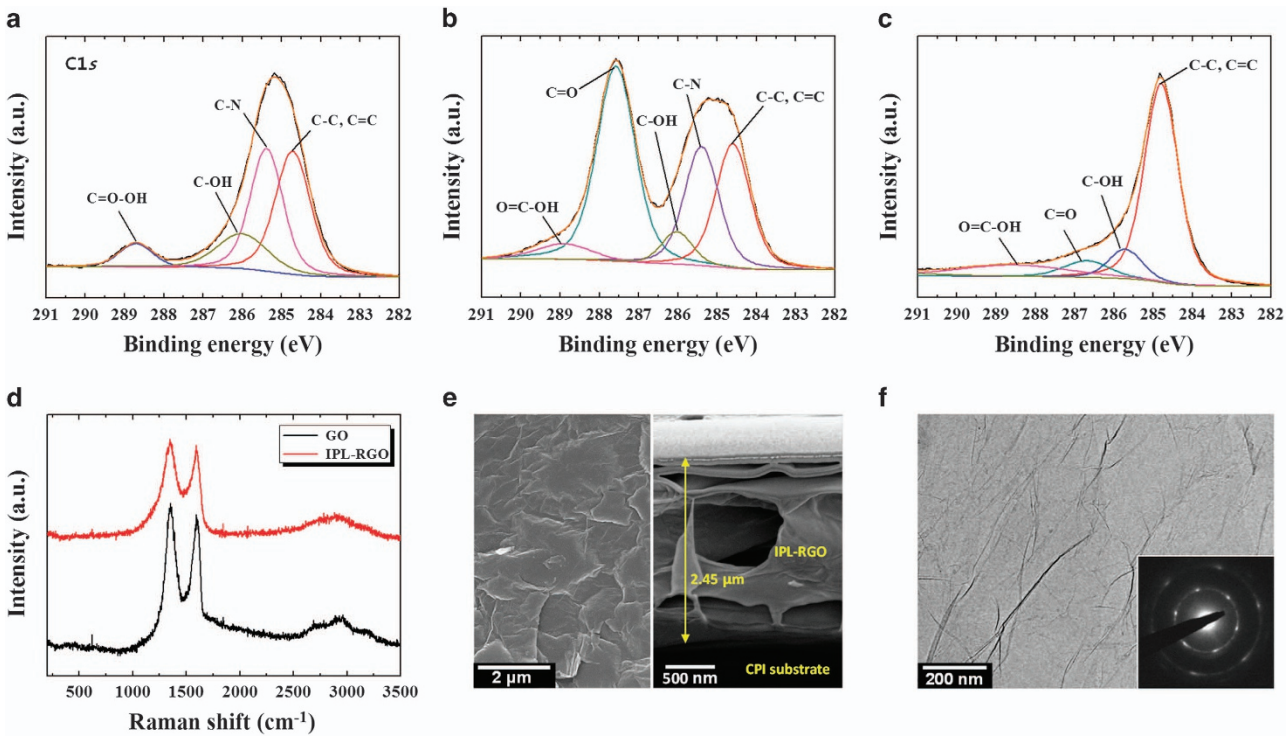

Figure 3 High resolution X-ray photoelectron spectroscopy (XPS) analysis at the vicinity of the C 1 *s* of (**a**) pristine CPI film and (**b**) GO and (**c**) intense pulsed light-reduced graphene oxide (IPL-RGO) sheets. (**d**) Raman spectroscopy analyses of GO and IPL-RGO sheets. (**e**) scanning electron microscopy analysis with the cross-sectional image and (**f**) transmission electron microscopy analysis of IPL-RGO sheets with selected area electron diffraction patterns in the inset of **f**.

and 1595 cm^{-1}, respectively. Although there were minor differences in the D/G intensity ratios (I_D/I_G) between the GO (1.10) and IPL-RGO sheets (1.05), the downward shift of the D band peak (1352 $cm^{-1} \rightarrow$ 1349 cm^{-1}) and the reduced intensity of the broad peak around 1700 cm^{-1} can explain the reduction of GO by the elimination of the functional groups and the restoration of the sp^2 network.[35] The morphological evolution of IPL-RGO sheets was investigated using scanning electron microscopy. After IPL irradiation, the RGO sheets exhibited a smaller dimensional size distribution (1–20 μm) and a rougher surface morphology, including the presence of multiple clusters, compared with the pristine GO sheets with slightly wrinkled morphology (Supplementary Figures S4 and S5 in the Supplementary Information). In addition, the IPL-RGO had an increased thickness of 2.45 μm compared with the 927-nm thickness of the pristine GO sheets due to the formation of open pores during the IPL irradiation (Figure 3e and Supplementary Figure S6 in the Supplementary Information). The generated pores enhanced the sensitivity toward chemical molecules by facilitating effective gas penetration. Transmission electron microscopy analysis revealed a two-dimensional planar structure of the IPL-RGO sheets with a characteristic hexagonal selected area electron diffraction pattern (Figure 3f and the inset of Figure 3f).

To investigate the real-time temperature transition during IPL exposure, we used an infrared camera (A655, FLIR; Figure 4). The infrared image showed an abrupt change in the temperature of the GO sheets (Figure 4a). A 0.3-factor slow speed video confirmed a sudden generation of heat in the pristine GO sheets and a subsequent recovery to ambient temperature (Supplementary Video 1). As shown in Figure 4b, the maximum temperature measured after the IPL irradiation was 490.7 °C, achieved within 16 msec. Subsequently, the generated heat was slowly cooled down to room temperature within 500 msec. The IPL is a very fascinating technique due to the ultrafast optical reduction of GO sheets in ambient air by heat generation using xenon flash light. This technique is applicable to a wide range of flexible and wearable electronics for modifying the electrical properties of graphene sheets without damaging the CPI substrate. Moreover, the development of transparent and flexible substrates with thermally stable CPI films is particularly important to sustain such high temperature over-shoots induced by IPL irradiation.

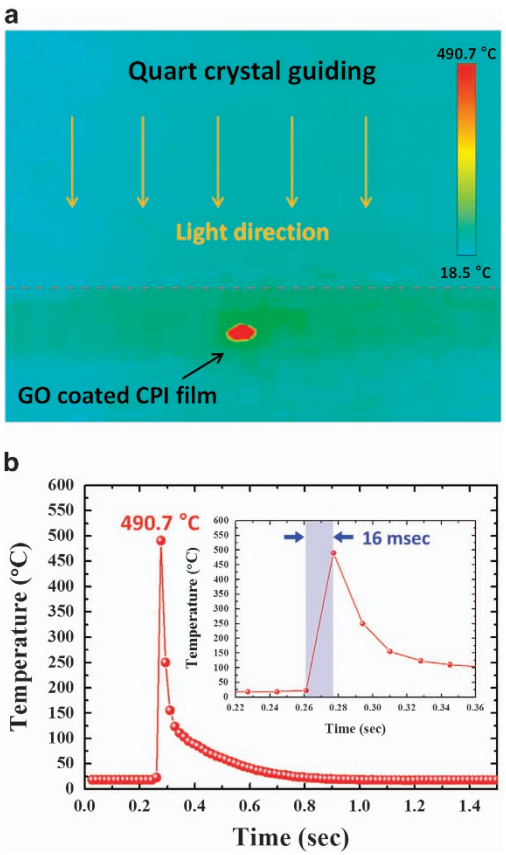

Figure 4 (**a**) Temperature gradient image captured by infrared camera during the intense pulsed light (IPL) irradiation of graphene oxide (GO)-coated colorless polyimide (CPI) film. (**b**) Real-time temperature transition of the GO sheets on CPI film during the IPL irradiation.

The gas sensing capabilities for hydrogen sulfide (H_2S), ethanol (C_2H_5OH) and hydrogen (H_2) of GO and IPL-RGO sheets coated on CPI films were evaluated at room temperature (Figure 5). The dynamic resistance changes toward 5–20 p.p.m. H_2S were investigated (Figure 5a). Highly stable response and recovery properties were observed with the IPL-RGO sensor. However, for the GO sensor, negligible resistance changes were observed during exposure to H_2S. The sensitivity was calculated from resistance values, that is, $[(R_{air}–R_{gas})/R_{air}] \times 100\%$ or $[(R_{gas}–R_{air})/R_{air}] \times 100\%$, where R_{air} and R_{gas} are the resistances of the IPL-RGO sensor when exposed to air and analyte gas, respectively. The average sensitivity ($[(R_{air}–R_{gas})/R_{air}] \times 100\%$) of the IPL-RGO sensor was 0.238% toward H_2S at 20 p.p.m. in the flat state (Figure 5b). A reduced sensitivity ($[(R_{gas}–R_{air})/R_{air}] \times 100\%$) was observed with an average value of 0.107% when the H_2S concentration dropped to 10 p.p.m. To demonstrate the mechanical stability of the IPL-RGO sensor on the CPI film, the sensing characteristics were evaluated in a bent state at an angle (θ_b) of 30° and in a flat state ($\theta_b = 0°$) (Supplementary Figure S7). Minor differences in sensitivity toward H_2S were observed between the flat (Figure 5b) and bent states (Figure 5c). The average sensitivity of the IPL-RGO sensor in the bent state was 0.224% toward H_2S at 20 p.p.m. (Figure 5c). The characteristic p–n transition was observed dependent on the H_2S concentration in both the flat and bending states. A characteristic n-type sensing property was observed using the IPL-RGO sensor for detecting 20 p.p.m. of H_2S, whereas a p-type sensing property was observed at the H_2S concentrations of 10 p.p.m. and 5 p.p.m. Similar p–n transitions in sensing characteristics were observed for the detection of C_2H_5OH and H_2 (Supplementary Figure S8). In the case of the GO sensor, there were no characteristic responses to analyte gases in both the flat and bent states (Supplementary Figure S9). Moreover, the GO sensor's sensing response was inconsistent without any identifiable trend. The long-term mechanical stability of the IPL-RGO sensor on CPI film was investigated by examining the resistance changes over a series of bending cycles (Figure 5d). There were minor resistance changes of less than ±3% variation from the initial resistance even after 10^4 bending cycles. The sensing properties before and after the bending cycles were evaluated for different analytes at 20 p.p.m. (Figure 5e). Consistent responses were obtained in the flat and bent states toward H_2S, C_2H_5OH, and H_2. Furthermore, the responses showed nearly negligible differences in the flat state after 10^4 bending cycles, demonstrating the long-term bending strain resistance of the IPL-RGO sensor.

The selective chemical detection property of the IPL-RGO sensor was further investigated for acetone (CH_3COCH_3), carbon monoxide (CO), toluene ($C_6H_5CH_3$) and methane (CH_4; Supplementary Figure S10). The IPL-RGO sensor exhibited relatively low sensitivity (~0.1%) even at high concentrations of 20 p.p.m. toward other interfering analytes. Based on the sensing results, the IPL-RGO sensor

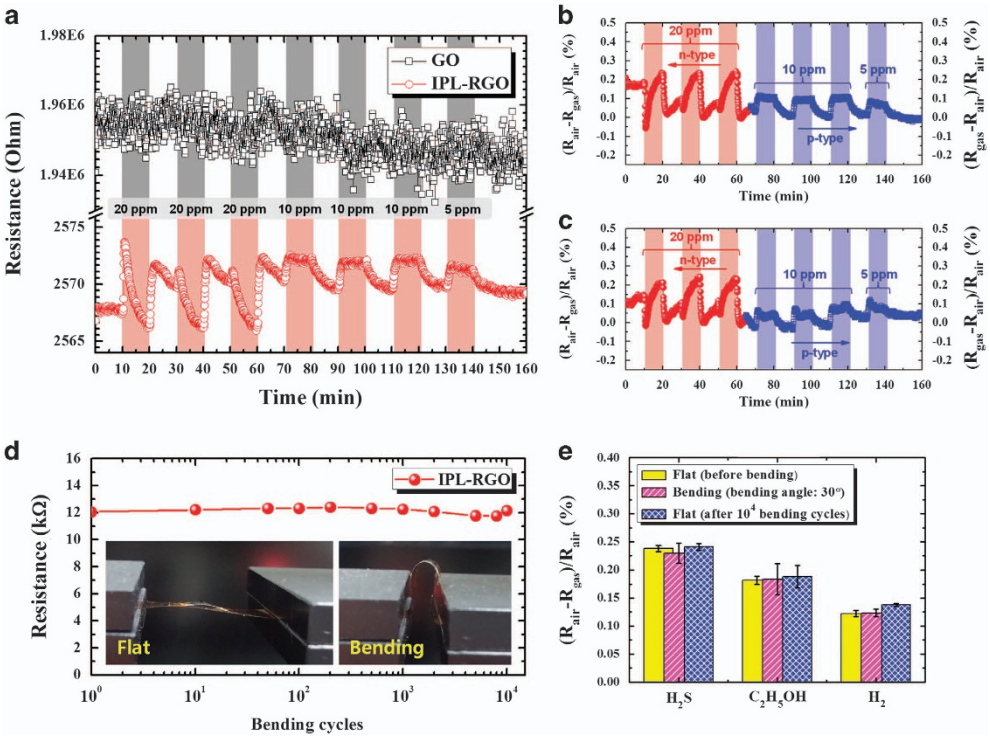

Figure 5 (**a**) Dynamic resistance transition of graphene oxide (GO) and intense pulsed light-reduced graphene oxide (IPL-RGO) sensors toward 5–20 p.p.m. H_2S at room temperature. Dynamic response transition of the IPL-RGO sensor to 5–20 p.p.m. H_2S at room temperature in (**b**) the flat state and (**c**) the bent state with a bending angle of 30°. (**d**) Resistance transition of the IPL-RGO sensor upon repeated bending cycles. (**e**) H_2S, ethanol and H_2 sensing performance of the IPL-RGO sensor at 20 p.p.m. before and after bending with a bending angle of 30°.

exhibited the most sensitive property toward H_2S at 20 p.p.m. (Supplementary Figure S11). The limit of detection of the IPL-RGO sensor was evaluated at 1–5 p.p.m. (Supplementary Figure S12). Characteristic p-type sensing properties were observed with noticeable sensitivity at 1 p.p.m. toward H_2S, acetone, ethanol, CO, H_2 and toluene. Ethanol particularly exhibited the highest sensitivity of 0.03% (Figure 6a). The stability of the IPL-RGO sensor was investigated by a series of measurements after 7 months (Figure 6b). Although the baseline resistance slightly increased to 6780 Ω compared with the 2568 Ω of an as-synthesized IPL-RGO sensor due to the oxidation in air, only minor differences in sensitivity (0.231%) were observed toward H_2S at 20 p.p.m. after 7 months. This demonstrated the long-term stability of the IPL-RGO sensor. The effect on the sensing property in humid ambient air was also investigated (Figure 6c and d). The baseline resistance changed from 1873.7 Ω in 1.5% RH ambient to 2722.4 Ω in 97% RH ambient (Figure 6c). In addition, the sensing property toward H_2S at 10 p.p.m. exhibited an opposite transition effect depending on the ambient humidity, that is, a p-type sensing property in dry conditions (1.5% RH) and an n-type sensing property in humid conditions (63% RH; Figure 6d). This transition was consistently observed even for the reactions toward ethanol and H_2 (Supplementary Figure S13). Although the baseline resistance shifted in humid ambient air, the IPL-RGO sensor exhibited stable sensing properties toward chemical species. Furthermore, the IPL-RGO sensor can be used for detecting humidity levels with further optimization.

To determine the feasibility for the selective detection of different chemical species using IPL-RGO sensors, a principal component analysis (PCA) was performed based on the measured sensitivities for gases at 5–20 p.p.m. in the flat and bent states (Figure 7). The PCA result demonstrated that the H_2S, C_2H_5OH and H_2 components were clustered in distinct regions without overlap, which confirmed the ability of the IPL-RGO sensors to distinguish three different gas species by pattern recognition. In addition, the clustered, distinct patterns were observed in both the flat and bent states. Thus, the IPL-RGO sensor can distinguish all three gas analytes even in the bent state. Moreover, other chemicals such as acetone, toluene, carbon monoxide and methane were also separated in the three-dimensional PCA domain.

The sensing mechanism and the improved sensing performance of IPL-RGO sheets compared with the pristine GO sheets are herein discussed (Figure 8). Generally, the analyte sensing property of graphene-based materials is attributed to charge transfer.[36] Graphene-based sensors exhibited a p-type semiconducting property during gas sensing.[37–39] For this reason, increasing resistance transitions occur resulting in p-type graphene sensors due to electron buildup from such reducing gases as H_2S.[39] In the present study, a similar p-type resistance transition occurred with IPL-RGO sheets toward 5–10 p.p.m. H_2S (Figure 8a). However, characteristic behaviors of a p–n transition were observed with the IPL-RGO sensor at relatively higher concentrations of H_2S. In other words, an n-type resistance transition occurred at 20 p.p.m. H_2S, indicating a decreasing resistance (Figure 8a). This behavior can be explained by the heavy doping of electrons from H_2S molecules during the H_2S exposure at high concentration, thereby converting the sensing characteristics of the IPL-RGO sensor from the p-type to the n-type (Figure 8b). Specifically, holes are the majority of carriers in the p-type IPL-RGO sensors during stabilization in ambient air (stage I). When reducing gas molecules such as H_2S were introduced to the IPL-RGO sensor, charge recombination between electrons and holes occurred due to the electron donating property of H_2S, which resulted in the sudden

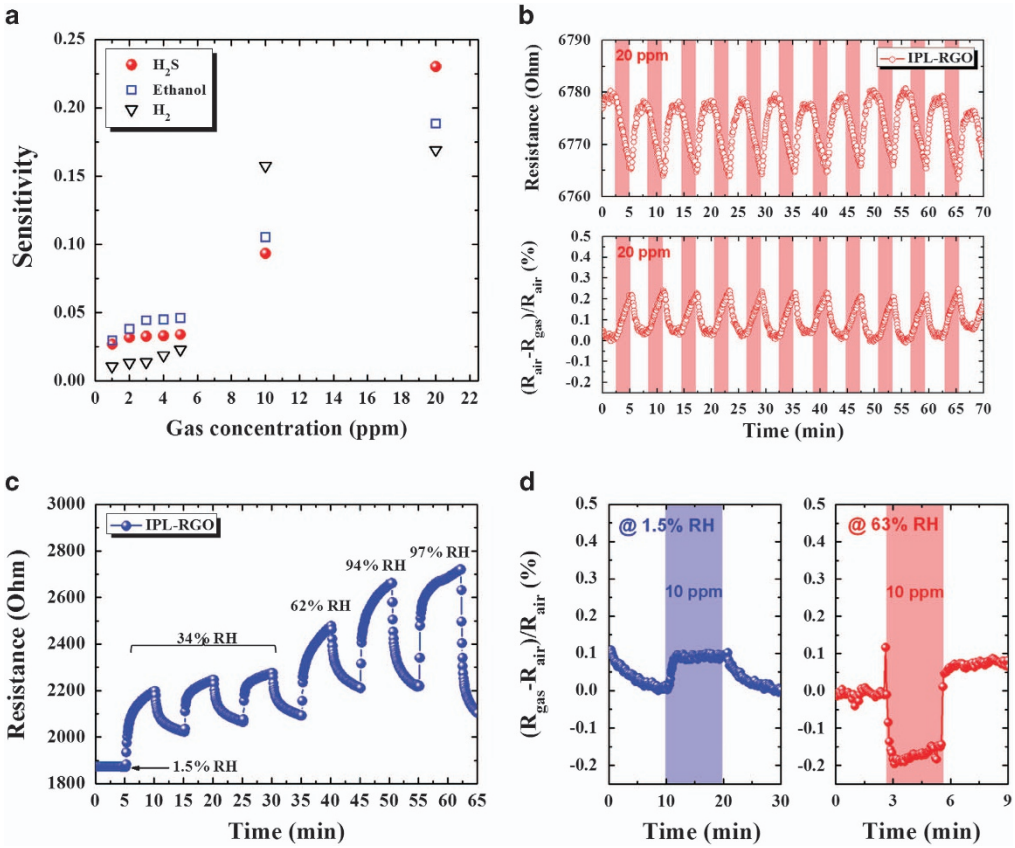

Figure 6 (**a**) Sensitivity values at different gas concentrations toward H_2S, ethanol and H_2. (**b**) Cyclic resistance and sensitivity transition of the intense pulsed light-reduced graphene oxide (IPL-RGO) sensor toward H_2S at 20 p.p.m. after 7 months. (**c**) Dynamic resistance transition of the IPL-RGO sensor at different relative humidity conditions. (**d**) Dynamic sensitivity transition of the IPL-RGO sensor toward H_2S at 10 p.p.m. in dry (1.5% RH) and humid (63% RH) conditions.

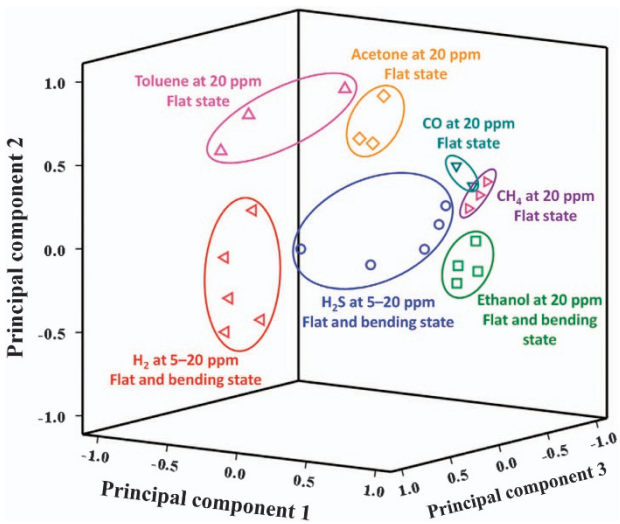

Figure 7 Principal component analysis for pattern recognition of H_2, H_2S, ethanol, acetone, toluene, carbon monoxide and methane at 5–20 p.p.m. using the intense pulsed light-reduced graphene oxide (IPL-RGO) sensor in the flat and bent states.

increase in resistance (stage II). However, a decreased resistance was observed just after the H_2S injection due to the p–n transition, wherein the majority of carriers were converted to electrons in IPL-RGO sheets (stage III). During the recovery process, the baseline resistance increased because a majority of the electrons disappeared due to the decreased H_2S concentration (stage IV). A further recovery process in ambient air resulted in the elimination of electrons and the regeneration of holes (stage V), which resulted in the n–p transition by converting the IPL-RGO sensor to a p-type sensor (stage VI). Interestingly, the simple p-type sensing characteristic was observed at lower H_2S concentrations below 10 p.p.m. without the p–n transition. Furthermore, the initial p-type IPL-RGO sensor in stage (I) was different from that in stage (VI), considering the increased baseline resistance in stage (VI) where the IPL-RGO sensor had a lower number of holes in stage (VI). The reduced hole concentration of the IPL-RGO sensor in stage (VI) was mainly attributed to the limited time for secondary recombination and hole generation. The p–n transitions in the IPL-RGO sheets were also observed during reactions with C_2H_5OH and H_2 because these molecules also have electron donating properties. Furthermore, this transition has also been observed in the literature. For example, R. Pearce *et al.* reported that epitaxially grown single-layered graphene on a SiC substrate exhibited p–n transitions at different NO_2 concentrations, which were attributed to electron donations from SiC and hole-doping from NO_2.[40,41] In addition, similar p–n transitions have been reported in chemiresistive sensors using SMOs at certain gas concentrations and operating temperatures.[42–44]

The improved analyte sensing performance of IPL-RGO sheets over the pristine GO sheets can be explained. First, IPL treatment enhanced the adhesion between the Au electrodes and IPL-RGO sheets.

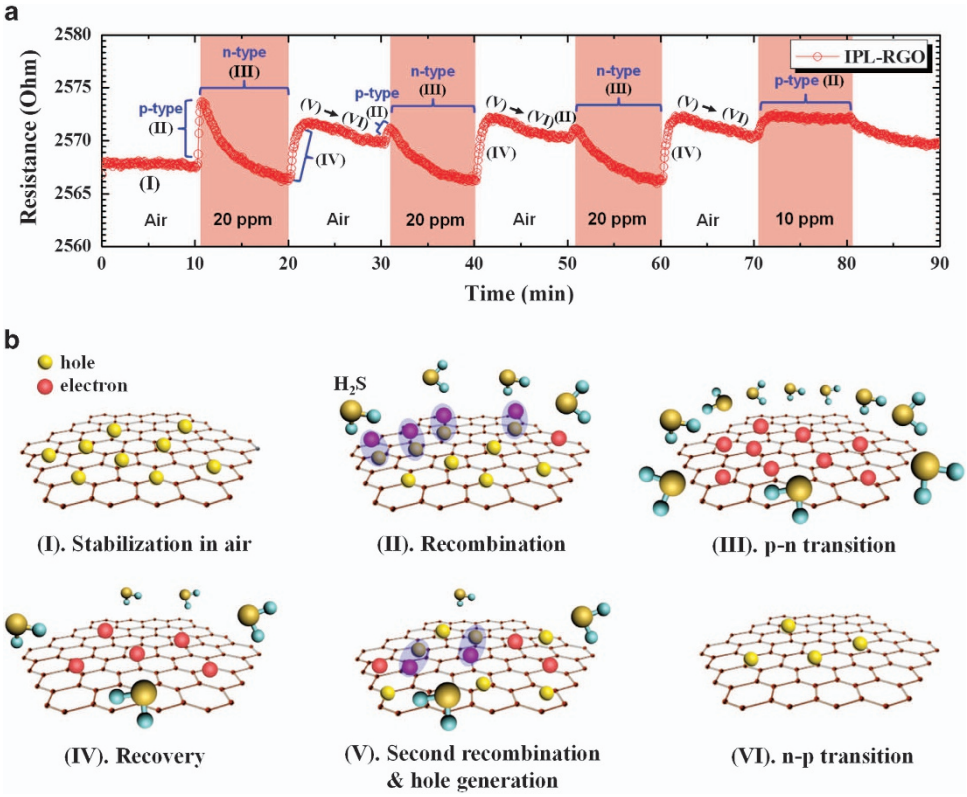

Figure 8 (**a**) Dynamic resistance change of intense pulsed light-reduced graphene oxide (IPL-RGO) sheets toward H_2S gas at 10 and 20 p.p.m. (**b**) Schematic illustrations of the sensing mechanism of IPL-RGO toward H_2S molecules; (I) stabilization in air, (II) recombination, (III) p–n transition, (IV) recovery, (V) second recombination and hole generation and (VI) n–p transition.

Figure 9 (**a**) Optical image of the wearable sensor module integrated with the intense pulsed light-reduced graphene oxide (IPL-RGO) sensor (blue dotted box). (**b**) Dynamic resistance transition of the IPL-RGO sensor on the wearable sensor module to 20 p.p.m. of H_2S at room temperature.

Typically, drop-casted GO exhibits weak binding forces between GO and the Au electrodes; this may account for the low signal-to-noise ratios during gas molecule sensing.[45] Improved adhesion properties can be achieved by the simultaneous robust optical sintering effect of intensive light-driven pulses and reduction of oxygen-containing functional groups on GO sheets. Second, the elimination of high-energy binding sites, such as vacancies and oxygen functional groups, can induce stable response and recovery characteristic of the IPL-RGO sensor. In a previous study, vacancies and oxygen functional groups resulted in slow sensor responses, whereas sp^2-bonded carbon provided rapid responses.[46] Thus, rapid responses and complete recovery could be achieved with IPL-RGO sheets. Furthermore, increasing the number of grain boundaries in the graphene sheet can enhance the analyte sensing property. Graphene with isolated grain boundaries exhibited a 300-times higher sensitivity to gas molecules than a single crystalline graphene grain.[47] Even though the polycrystalline graphene showed a lower sensitivity than an isolated grain boundary, the improvement in sensitivity was noticeable. In the present study, morphological observations revealed an increased number of grains in the IPL-RGO sheets after IPL irradiation (Figure 3e) relative to GO sheets, which exhibited large grains with densely packed structures (Supplementary Figures S4 and S5). For this reason, the large number of grain boundaries in the IPL-RGO and the formation of multiple stacking structures induced enhanced sensing responses. Finally, IPL-RGO sheets exhibited interlayer pores between the IPL-RGO domains formed by intensively irradiated light (Figure 3e). As a result, the surface reactions on IPL-RGO sheets could be activated by effective and facile gas penetration into the inner layers of IPL-RGO sheets. Other possible reasons for the improved chemical sensing properties of IPL-RGO can

be interpreted by the enhanced electrical conductivity[37] and the formation of ohmic contacts between the Au electrodes and the IPL-RGO sheets.[39,48]

We further developed wearable watch-type sensing modules that can transmit data to a smartphone using Bluetooth-assisted wireless communication (Figure 9). An IPL-RGO sensor was integrated with the wearable sensor module (blue-dotted box in Figure 9a) and mounted on a flexible printed circuit board. The measurement was performed by applying 3 V between the patterned IDEs to determine the resistance changes when H_2S was injected at the IPL-RGO sensor (Figure 9b). Multiple cyclic exposures to 20 p.p.m. of H_2S and to fresh air were carried out for 90 s each. The results showed stable and consistent resistance changes for 7 cyclic H_2S exposures at room temperature. This demonstrated a portable application of the IPL-RGO sensor as a real-time environmental monitor.

CONCLUSION

In this work, for the first time, we demonstrated a facile and ultrafast optical reduction of GO sheets without any thermal damage to an underlying CPI substrate. These composite films have potential applications as wearable chemical sensors. Highly transparent and thermally stable CPI film was synthesized by combining anhydride and diamine monomers containing trifluoromethyl ($–CF_3$) and sulfone ($–SO_2$) groups. The electrical properties of GO coated on the CPI substrate were optically tuned by IPL irradiation, resulting in the formation of RGO sheets (IPL-RGO). An ~100-fold improvement in electrical conductivity was obtained within 4 msec, which was attributed to the ultrafast reduction of GO sheets. IPL-RGO formation was confirmed by analyzing the chemical binding states using XPS and Raman spectroscopy. The IPL-RGO sheets on CPI substrates exhibited stable analyte sensing performance with high response toward H_2S, ethanol and H_2. In particular, a high resistance transition up to 0.238% and a stable recovery were observed for 20 p.p.m. H_2S. Moreover, consistent sensing properties were maintained even in bent states with a 30° bending angle up to 10^4 bending cycles. This demonstrated a long-term bending strain resistance. Furthermore, selective and distinct pattern recognition of H_2S, C_2H_5OH and H_2 gases was demonstrated by PCA. Finally, the IPL-RGO was coated onto CPI films and successfully integrated with wearable sensor modules for applications in real-time health and environmental monitors.

CONFLICT OF INTEREST

The authors declare no conflict of interest.

ACKNOWLEDGEMENTS

This work was supported by Wearable Platform Materials Technology Center (WMC) funded by the National Research Foundation of Korea (NRF) Grant of the Korean Government (MSIP; No. 2016R1A5A1009926). This work was also supported by the Korea Institute of Machinery & Materials (KIMM) and the National Research Council of Science and Technology (NST), Republic of Korea. We would like to thank Da Som Lee for her support in the fabrication of the CPI films.

1 Windmiller, J. R. & Wang, J. Wearable electrochemical sensors and biosensors: a review. *Electroanal* **25**, 29–46 (2013).
2 Kim, D. H., Lu, N. S., Ma, R., Kim, Y. S., Kim, R. H., Wang, S. D., Wu, J., Won, S. M., Tao, H., Islam, A., Yu, K. J., Kim, T. I., Chowdhury, R., Ying, M., Xu, L. Z., Li, M., Chung, H. J., Keum, H., McCormick, M., Liu, P., Zhang, Y. W., Omenetto, F. G., Huang, Y. G., Coleman, T. & Rogers, J. A. Epidermal electronics. *Science* **333**, 838–843 (2011).
3 Amjadi, M., Kyung, K.-U., Park, I. & Sitti, M. Stretchable, skin-mountable, and wearable strain sensors and their potential applications: a review. *Adv. Funct. Mater.* **26**, 1678–1698 (2016).
4 Zhong, J. W., Zhang, Y., Zhong, Q. Z., Hu, Q. Y., Hu, B., Wang, Z. L. & Zhou, J. Fiber-based generator for wearable electronics and mobile medication. *ACS Nano* **8**, 6273–6280 (2014).
5 Kim, K. K., Hong, S., Cho, H. M., Lee, J., Suh, Y. D., Ham, J. & Ko, S. H. Highly sensitive and stretchable multidimensional strain sensor with prestrained anisotropic metal nanowire percolation networks. *Nano Lett.* **15**, 5240–5247 (2015).
6 Yamada, T., Hayamizu, Y., Yamamoto, Y., Yomogida, Y., Izadi-Najafabadi, A., Futaba, D. N. & Hata, K. A stretchable carbon nanotube strain sensor for human-motion detection. *Nat. Nanotechnol.* **6**, 296–301 (2011).
7 Kim, S. Y., Park, S., Park, H. W., Park, D. H., Jeong, Y. & Kim, D. H. Highly sensitive and multimodal all-carbon skin sensors capable of simultaneously detecting tactile and biological stimuli. *Adv. Mater.* **27**, 4178–4185 (2015).
8 Gong, S., Schwalb, W., Wang, Y. W., Chen, Y., Tang, Y., Si, J., Shirinzadeh, B. & Cheng, W. L. A wearable and highly sensitive pressure sensor with ultrathin gold nanowires. *Nat. Commun.* **5**, 3132 (2014).
9 Lipomi, D. J., Vosgueritchian, M., Tee, B. C. K., Hellstrom, S. L., Lee, J. A., Fox, C. H. & Bao, Z. N. Skin-like pressure and strain sensors based on transparent elastic films of carbon nanotubes. *Nat. Nanotechnol.* **6**, 788–792 (2011).
10 Bai, S. L., Sun, C. Z., Wan, P. B., Wang, C., Luo, R. X., Li, Y. P., Liu, J. F. & Sun, X. M. Transparent conducting films of hierarchically nanostructured polyaniline networks on flexible substrates for high-performance gas sensors. *Small* **11**, 306–310 (2015).
11 Mirica, K. A., Weis, J. G., Schnorr, J. M., Esser, B. & Swager, T. M. Mechanical drawing of gas sensors on paper. *Angew. Chem. Int. Ed.* **51**, 10740–10745 (2012).
12 Kim, I. D., Rothschild, A. & Tuller, H. L. Advances and new directions in gas-sensing devices. *Acta Mater.* **61**, 974–1000 (2013).
13 Choi, S. J., Kim, S. J., Cho, H. J., Jang, J. S., Lin, Y. M., Tuller, H. L., Rutledge, G. C. & Kim, I. D. WO_3 nanofiber-based biomarker detectors enabled by protein-encapsulated catalyst self-assembled on polystyrene colloid templates. *Small* **12**, 911–920 (2016).
14 Choi, S. J., Choi, C., Kim, S. J., Cho, H. J., Hakim, M., Jeon, S. & Kim, I. D. Highly efficient electronic sensitization of non-oxidized graphene flakes on controlled pore-loaded WO_3 nanofibers for selective detection of H_2S molecules. *Sci. Rep.* **5**, 8067 (2015).
15 Shin, J., Choi, S. J., Lee, I., Youn, D. Y., Park, C. O., Lee, J. H., Tuller, H. L. & Kim, I. D. Thin-wall assembled SnO_2 fibers functionalized by catalytic Pt nanoparticles and their superior exhaled-breath-sensing properties for the diagnosis of diabetes. *Adv. Funct. Mater.* **23**, 2357–2367 (2013).
16 Choi, H., Choi, J. S., Kim, J. S., Choe, J. H., Chung, K. H., Shin, J. W., Kim, J. T., Youn, D. H., Kim, K. C., Lee, J. I., Choi, S. Y., Kim, P., Choi, C. G. & Yu, Y. J. Flexible and transparent gas molecule sensor integrated with sensing and heating graphene layers. *Small* **10**, 3685–3691 (2014).
17 Lee, J. S., Oh, J., Jun, J. & Jang, J. Wireless hydrogen smart sensor based on Pt/graphene-immobilized radio-frequency identification tag. *ACS Nano* **9**, 7783–7790 (2015).
18 Duy, L. T., Kim, D. J., Trung, T. Q., Dang, V. Q., Kim, B. Y., Moon, H. K. & Lee, N. E. High performance three-dimensional chemical sensor platform using reduced graphene oxide formed on high aspect-ratio micro-pillars. *Adv. Funct. Mater.* **25**, 883–890 (2015).
19 Wang, D. H., Hu, Y., Zhao, J. J., Zeng, L. L., Tao, X. M. & Chen, W. Holey reduced graphene oxide nanosheets for high performance room temperature gas sensing. *J. Mater. Chem. A* **2**, 17415–17420 (2014).
20 Yuan, W. J., Liu, A. R., Huang, L., Li, C. & Shi, G. Q. High-performance NO_2 sensors based on chemically modified graphene. *Adv. Mater.* **25**, 766–771 (2013).
21 Tian, H., Chen, H. Y., Ren, T. L., Li, C., Xue, Q. T., Mohammad, M. A., Wu, C., Yang, Y. & Wong, H. S. P. Cost-effective, transfer-free, flexible resistive random access memory using laser-scribed reduced graphene oxide patterning technology. *Nano Lett.* **14**, 3214–3219 (2014).
22 Kymakis, E., Savva, K., Stylianakis, M. M., Fotakis, C. & Stratakis, E. Flexible organic photovoltaic cells with in situ nonthermal photoreduction of spin-coated graphene oxide electrodes. *Adv. Funct. Mater.* **23**, 2742–2749 (2013).
23 Yang, S. B., Choi, H., Lee, D. S., Choi, C. G., Choi, S. Y. & Kim, I. D. Improved optical sintering efficiency at the contacts of silver nanowires encapsulated by a graphene layer. *Small* **11**, 1293–1300 (2015).
24 Yang, H. Y., Hong, J. M., Kim, T. W., Song, Y. W., Choi, W. K. & Lim, J. A. Split-second nanostructure control of a polymer:fullerene photoactive layer using intensely pulsed white light for highly efficient production of polymer solar cells. *ACS Appl. Mater. Interfaces* **6**, 1495–1501 (2014).
25 Park, S. H. & Kim, H. S. Environmentally benign and facile reduction of graphene oxide by flash light irradiation. *Nanotechnology* **26**, 205601 (2015).
26 Guo, Y. L., Wu, B., Liu, H. T., Ma, Y. Q., Yang, Y., Zheng, J., Yu, G. & Liu, Y. Q. Electrical assembly and reduction of graphene oxide in a single solution step for use in flexible sensors. *Adv. Mater.* **23**, 4626–4630 (2011).
27 Yang, G., Lee, C., Kim, J., Ren, F. & Pearton, S. J. Flexible graphene-based chemical sensors on paper substrates. *Phys. Chem. Chem. Phys.* **15**, 1798–1801 (2013).
28 Cho, B., Yoon, J., Lim, S. K., Kim, A. R., Kim, D. H., Park, S. G., Kwon, J. D., Lee, Y. J., Lee, K. H., Lee, B. H., Ko, H. C. & Hahm, M. G. Chemical sensing of 2D graphene/MoS_2 heterostructure device. *ACS Appl. Mater. Interfaces* **7**, 16775–16780 (2015).
29 Claramunt, S., Monereo, O., Boix, M., Leghrib, R., Prades, J. D., Cornet, A., Merino, P., Merino, C. & Cirera, A. Flexible gas sensor array with an embedded heater based on metal decorated carbon nanofibres. *Sens. Actuators B* **187**, 401–406 (2013).

30 Hasegawa, T. & Horie, K. Photophysics, photochemistry, and optical properties of polyimides. *Prog. Polym. Sci.* **26**, 259–335 (2001).
31 Choi, I. H. & Chang, J. H. Colorless polyimide nanocomposite films containing hexafluoroisopropylidene group. *Polym. Adv. Technol.* **22**, 682–689 (2011).
32 Yavari, F., Chen, Z. P., Thomas, A. V., Ren, W. C., Cheng, H. M. & Koratkar, N. High sensitivity gas detection using a macroscopic three-dimensional graphene foam network. *Sci. Rep.* **1**, 166 (2011).
33 Dreyer, D. R., Park, S., Bielawski, C. W. & Ruoff, R. S. The chemistry of graphene oxide. *Chem. Soc. Rev.* **39**, 228–240 (2010).
34 Eda, G. & Chhowalla, M. Chemically derived graphene oxide: towards large-area thin-film electronics and optoelectronics. *Adv. Mater.* **22**, 2392–2415 (2010).
35 Lorenzoni, M., Giugni, A., Di Fabrizio, E., Perez-Murano, F., Mescola, A. & Torre, B. Nanoscale reduction of graphene oxide thin films and its characterization. *Nanotechnology* **26**, 285301 (2015).
36 Kim, J., Kwon, S., Cho, D. H., Kang, B., Kwon, H., Kim, Y., Park, S. O., Jung, G. Y., Shin, E., Kim, W. G., Lee, H., Ryu, G. H., Choi, M., Kim, T. H., Oh, J., Park, S., Kwak, S. K., Yoon, S. W., Byun, D., Lee, Z. & Lee, C. Direct exfoliation and dispersion of two-dimensional materials in pure water via temperature control. *Nat. Commun.* **6**, 8294 (2015).
37 Joshi, R. K., Gomez, H., Alvi, F. & Kumar, A. Graphene Films and Ribbons for Sensing of O_2, and 100 p.p.m. of CO and NO_2 in Practical Conditions. *J. Phys. Chem. C* **114**, 6610–6613 (2010).
38 Lu, G. H., Ocola, L. E. & Chen, J. H. Reduced graphene oxide for room-temperature gas sensors. *Nanotechnology* **20**, 445502 (2009).
39 Fowler, J. D., Allen, M. J., Tung, V. C., Yang, Y., Kaner, R. B. & Weiller, B. H. Practical chemical sensors from chemically derived graphene. *ACS Nano* **3**, 301–306 (2009).
40 Yuan, W. J. & Shi, G. Q. Graphene-based gas sensors. *J. Mater. Chem. A* **1**, 10078–10091 (2013).
41 Pearce, R., Iakimov, T., Andersson, M., Hultman, L., Spetz, A. L. & Yakimova, R. Epitaxially grown graphene based gas sensors for ultra sensitive NO_2 detection. *Sens. Actuators B* **155**, 451–455 (2011).
42 Dai, Z., Lee, C. S., Tian, Y., Kim, I. D. & Lee, J. H. Highly reversible switching from P- to N-type NO_2 sensing in a monolayer Fe_2O_3 inverse opal film and the associated P-N transition phase diagram. *J. Mater. Chem. A* **3**, 3372–3381 (2015).
43 Wang, J. X., Sun, X. W., Yang, Y. & Wu, C. M. L. N-P transition sensing behaviors of ZnO nanotubes exposed to NO_2 gas. *Nanotechnology* **20**, 465501 (2009).
44 Kim, I. D., Rothschild, A., Lee, B. H., Kim, D. Y., Jo, S. M. & Tuller, H. L. Ultrasensitive chemiresistors based on electrospun TiO_2 nanofibers. *Nano Lett.* **6**, 2009–2013 (2006).
45 Kim, Y. H., Kim, S. J., Kim, Y. J., Shim, Y. S., Kim, S. Y., Hong, B. H. & Jang, H. W. Self-activated transparent all-graphene gas sensor with endurance to humidity and mechanical bending. *ACS Nano* **9**, 10453–10460 (2015).
46 Kumar, B., Min, K., Bashirzadeh, M., Farimani, A. B., Bae, M. H., Estrada, D., Kim, Y. D., Yasaei, P., Park, Y. D., Pop, E., Aluru, N. R. & Salehi-Khojin, A. The role of external defects in chemical sensing of graphene field-effect transistors. *Nano Lett.* **13**, 1962–1968 (2013).
47 Yasaei, P., Kumar, B., Hantehzadeh, R., Kayyalha, M., Baskin, A., Repnin, N., Wang, C. H., Klie, R. F., Chen, Y. P., Kral, P. & Salehi-Khojin, A. Chemical sensing with switchable transport channels in graphene grain boundaries. *Nat. Commun.* **5**, 4911 (2014).
48 Choi, Y. R., Yoon, Y. G., Choi, K. S., Kang, J. H., Shim, Y. S., Kim, Y. H., Chang, H. J., Lee, J. H., Park, C. R., Kim, S. Y. & Jang, H. W. Role of oxygen functional groups in graphene oxide for reversible room-temperature NO_2 sensing. *Carbon* **91**, 178–187 (2015).

Supplementary Information accompanies the paper on the NPG Asia Materials website (http://www.nature.com/am)